Direct imaging of antiferromagnet-ferromagnet phase transition in van der Waals antiferromagnet CrSBr

Jingjing Yu,[†] Daxiang Liu,[†] Zhenyu Ding,[†] Yanan Yuan, Jiayuan Zhou, Fangfang Pei, Haolin Pan, Tianping Ma, Feng Jin, Lingfei Wang, Wenguang Zhu, Shouguo Wang, Yizheng Wu, Xue Liu, Dazhi Hou, Yang Gao, Ziqiang Qiu, Mengmeng Yang,* and Qian Li**

[†] These authors contributed equally

J. J. Yu, J. Y. Zhou, X. Liu, M. M. Yang

Institute of Physical Science and Information Technology

Anhui University

Hefei, Anhui 230601, China

E-mail: mmyangphy@ahu.edu.cn

D. X. Liu, Y. N. Yuan, F. F. Pei, Q. Li

National Synchrotron Radiation Laboratory

School of Nuclear Science and Technology

University of Science and Technology of China

Hefei, Anhui 230026, China

This is the author manuscript accepted for publication and has undergone full peer review but has not been through the copyediting, typesetting, pagination and proofreading process, which may lead to differences between this version and the Version of Record. Please cite this article as doi: 10.1002/adfm.202307259.

E-mail: liqian89@ustc.edu.cn

Z. Y. Ding, H. L. Pan, L. F. Wang, F. Jin, W. G. Zhu, D. Z. Hou,

Hefei National Research Center for Physical Sciences at the Microscale

University of Science and Technology of China

Hefei, Anhui 230026, China

T. P. Ma, S. G. Wang,

School of Materials Science and Engineering Department

Anhui University

Hefei, Anhui 230601, China

W. G. Zhu, Y. Gao,

CAS Key Laboratory of Strongly-Coupled Quantum Matter Physics

Department of Physics

University of Science and Technology of China

Hefei 230601, China

Y. Z. Wu,

Department of Physics

State Key Laboratory of Surface Physics

Fudan University

Shanghai 200433, China

Z. Q. Qiu,

Department of Physics

University of California at Berkeley

Berkeley, California 94720, USA

E-mail: qiu@berkeley.edu

Keywords: van der Waals antiferromagnet, direct imaging of AFM Néel vector orientation, magneto-optic anisotropy, antiferromagnet-ferromagnet phase transition, spin-flop state

Abstract

The advent of van der Waals (vdW) ferromagnetic (FM) and antiferromagnetic (AFM) materials offers unprecedented opportunities for spintronics and magneto-optic devices. Combining magnetic Kerr microscopy and density functional theory calculations, we investigate the AFM-FM transition and discover a surprising abnormal magneto-optic anisotropy in vdW CrSBr associated to different magnetic phases (FM, AFM, or paramagnetic state). This unique magneto-optic property leads to different anisotropic optical reflectivity from different magnetic states, permitting direct imaging of the AFM Néel vector orientation and the dynamic process of the AFM-FM transition within a magnetic field. Using Kerr microscopy, we not only image the domain nucleation and propagation process but also identify the intermediate spin-flop state in the AFM-FM transition. The unique

magneto-optic property and clear identification of the dynamics process of the AFM-FM phase transition in CrSBr demonstrate the promise of vdW magnetic materials for future spintronic technology.

1. Introduction

Since the discovery of a long-range magnetic order in two-dimensional $Cr_2Ge_2Te_6$[1] and CrI_3,[2] van der Waals (vdW) magnets have drawn great interest because they can be easily exfoliated down into a monolayer while retaining the magnetic order. Compared with conventional magnets, vdW magnets show larger response under the application of strain,[3] pressure,[4] doping,[5,6] and voltage gating,[7] exhibiting excellent magneto-electrical properties,[8-10] intriguing magneto-optical properties,[11,12] and fascinating topological magnetic structures.[13,14] As a counter partner of ferromagnetic (FM) materials, antiferromagnets (AFM) have drawn enormous attention during the past decade due to their robustness against magnetic fields, no stray fields, ultrafast dynamics, etc.[15,16] Thus, it is desirable to realize AFM-FM dual states in the same materials to establish the importance of both FM and AFM materials. However, unfortunately, it is almost impossible to align AFM order into FM order by applying an easily reachable magnetic field in conventional AFM materials.[17,18] vdW AFM materials offer a unique opportunity because of their much weaker interlayer coupling than intralayer coupling. In vdW AFM materials that have FM order in each layer but AFM order between the nearest neighbor layers, it is possible to switch the vdW AFM order into the FM order by applying a magnetic field to overcome interlayer coupling.[2,4,5,8,11]

Among these vdW AFM materials, CrSBr[19-27] has stood out recently due to its high air stability, high Néel temperature (T_N=132 K), high bulk Curie temperature (T_C~160 K), A-type antiferromagnet (AFM), semiconductivity and etc. Each rectangular layer (Figure 1A) of the vdW CrSBr exhibits an in-plane anisotropic FM order. These FM layers couple antiferromagnetically along the stacking direction. In particular, the exfoliated CrSBr flake exhibits a rectangular shape with long edge points along the a-axis and short edge points along the b-axis (easy spin axis).[21-26]. With a semiconducting bandgap and

a strong magnetic order-tailored interlayer electronic coupling, CrSBr has been demonstrated to show unique properties in the characterization of Raman spectroscopy,[26] photoluminescence,[23] second harmonic generation,[21] magnetoresistance,[22] and electronic transport[24] experiments.

As a basic first-order phase transition phenomenon, the investigation of AFM-FM transition and spin-flop transition in AFM has been hindered in the long term by a high critical magnetic field,[17,18] multidomain structure,[28,29] lack of technique to directly determine the compensated Néel vectors and more. The relatively weak antiferromagnetic interlayer coupling[19,20] in CrSBr yields a small magnetic field for AFM-FM phase transition and the spin-flop.[21-26] Moreover, CrSBr exhibits a single domain with Néel vector along the well-defined b-axis, which establishes CrSBr as an ideal candidate to study the magnetic order-related phenomenon. Recent magneto-transport measurements have reported layer-dependent interlayer spin reorientation by speculating from the plateaus of resistance results and numerical calculation.[30] Controversies regarding the positive or negative magnetoresistance in CrSBr, especially field-induced spin reorientation, have been raised.[22,25,30] Previous literature has revealed inhomogeneous AFM-FM phase transformation at different regions of the sample and multiple domain evolution modes in FeRh,[31,32] and antiferromagnetically coupled multilayers.[33] However, spatially-resolved direct imaging of field-induced spin reorientation and the dynamic process of AFM-FM transition in CrSBr has been lacking thus far.

The absence of a net magnetic moment makes the direct determination of the AFM Néel vector quite challenging. Utilizing X-ray linear dichroism effect, photoemission electron microscopy (PEEM) was used to image the AFM domains.[34,35] Unfortunately, PEEM does not allow the simultaneous application of magnetic fields and domain imaging, leaving the investigation of magnetic field-driven AFM-FM phase transitions to resort to other techniques. Neither the spin-polarized scanning tunneling microscopy[36,37] nor magnetic force microscopy[38,39] could easily offer the imaging of compensated AFM Néel vector reorientation under an in-plane scanning magnetic field. Previous studies have reported anisotropic electronic conductivity between the in-plane a-axis and b-axis[25] and an abrupt switch in the photoluminescence spectra from AFM to FM order,[23] suggesting the possibility to determining the Néel vector magneto-optically and directly imaging the AFM-FM phase transition of CrSBr. The direct determination of the compensated AFM Néel vector was realized

through the magneto-optical Voigt effect or the optical birefringence effect in CuMnAs,[40] NiO[41] and CoO.[42] Here by using a magneto-optic Kerr microscope, we demonstrated the direct imaging of AFM order and AFM-FM phase transition in vdW AFM CrSBr. Combining the properties of 2D vdW materials and AFM characteristics, CrSBr offers great potential for future 2D AFM spintronics and device applications.

2. Results and discussions

2.1 Magnetic order-dependent magneto-optical Kerr signal

In this work, we first investigated the macroscopic magnetization of CrSBr as a function of the magnetic field using a vibrating sample magnetometer (VSM) and the magneto-optic Kerr effect (MOKE).[43] CrSBr single crystals were synthesized using a chemical vapor transport method [Experimental Section] ~~[Materials and Methods]~~.[30] We mechanically exfoliated a flat CrSBr crystal from the bulk crystal and stamped it onto a silicon wafer for VSM and MOKE characterization. The M-H loops obtained by VSM at three measurement geometries (Figure 1B-D) clearly showed the anisotropic magneto-crystalline properties of CrSBr, where the in-plane b-axis is the easy axis and in-plane a-axis and out-of-plane c-axis are the secondary easy and hard axis, respectively. In contrast to the VSM result, which showed the expected antisymmetric shape of the hysteresis loop (e.g., opposite saturation magnetizations at opposite saturation magnetic fields), the Kerr signal (Figure 1E) from the same CrSBr crystals exhibited an almost symmetric shape of the hysteresis loop (e.g., identical saturation Kerr values at opposite saturation magnetic fields) below its Néel temperature (T_N~132 K) (Figure 1F-H). This is particularly evidenced by the sudden jump of the Kerr signal at the AFM-FM phase transition for H//b axis (Figure 1G) and by a continuous change in the Kerr signal for H//a axis (Figure 1F) and H//c axis (Figure 1H) below the T_N. With increasing temperature, both the longitudinal Kerr signals for H//b axis (Figure 1G) and H//a axis (Figure 1F) become an almost flat line above T_N, where the AFM order between different layers vanishes. For H//c axis (Figure 1H), the polar MOKE signal is dominated by symmetric shape below T_N and changes to the normal hysteresis loop shape for temperature above T_N but below its T_C ($T_N<T<T_C$~160 K). The above results confirm that the Kerr signal from CrSBr below T_N is dominated by the states of AFM or FM order between adjacent layers rather

than by the sign of net magnetization. In other words, the sign of the magnetization along one axis contribute much less to the Kerr signal than the magnetic ordering state which corresponds to the AFM-FM transition of CrSBr.

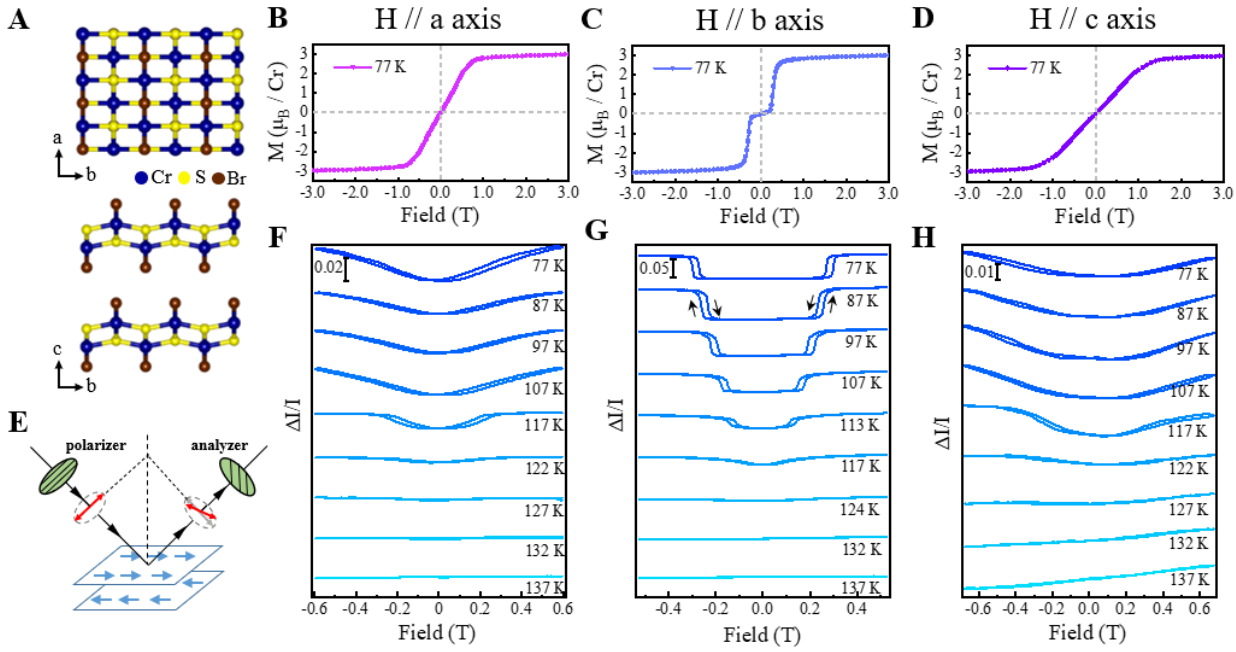

Figure 1. Structure and magneto-optic properties of CrSBr. A) Crystal structures of CrSBr with the top and bottom images show the top view and side view of the structure. Hysteresis loop at 77 K measured by VSM with magnetic field along B) a axis, C) b axis, and D) c axis of CrSBr. E) Schematic drawing of the measurement geometry for longitudinal MOKE in F) and G) with p-polarized incident light. H) is measured in polar MOKE geometry with normal incident light. Magneto-optic Kerr signal as a function of magnetic field covering a temperature range from 77 K to 137 K with field along (F) a axis, (G) b axis and (H) c axis, where ΔI/I is defined as the change of amplitude of measured light intensity over the average intensity value during one cycle of field sweeping process.

2.2 Anisotropic reflectivity of antiferromagnetic, ferromagnetic and paramagnetic CrSBr

Generally, the MOKE signal is determined by the dielectric tensor, with the diagonal symmetric elements determining the reflectivity and the antisymmetric off-diagonal elements determining the antisymmetric hysteresis loop from the net FM magnetization.[43] The MOKE result in Figure 1 indicates that the MOKE signal in CrSBr is dominated by the symmetric elements of the dielectric tensor as opposed to the antisymmetric off-diagonal elements of the dielectric tensor in ordinary magnetic materials. This result is in good agreement with the magnetic space group analysis, in that the antisymmetric off-diagonal elements are zero [Experimental Section~~Materials and Methods~~]. Since symmetric dielectric tensor is diagonalized in the frame of principal axes, a- and b-axis, in the CrSBr crystal,[41,42] the symmetric MOKE loops in Figure 1 must have originated from different dielectric constants along the a- and b-axis in CrSBr (e.g., $\varepsilon_a \neq \varepsilon_b$, where ε_a and ε_b are the dielectric constants for polarization parallel to the a- and b-axis, respectively), which had the same origin with optical birefringence. To confirm this theoretical analysis, we performed polarization-dependent reflectivity measurements on the AFM, FM, and paramagnetic (PM) phases of CrSBr to explore the magnetic order-dependent diagonal part of the dielectric tensor or optical conductivity. The optical images of two CrSBr samples with orthogonally aligned crystal axes and with normal incident light (Figure 2A-F) were taken simultaneously to exclude the background of polarization-dependent intensity of incident light. Indeed, we found the anisotropic reflectivity at different polarizations of incident light for CrSBr samples in all magnetic phases here. In the AFM phase (Figure 2A, B) and FM phase (Figure 2C, D) at 77 K, samples A and B exhibited obviously different reflectivity. In the PM phase at 300 K (Figure 2E, F), the CrSBr showed reversed contrast for samples A and B as compared to those in the AFM and FM phases.~~, indicating that the magnetic order-dependent reflectivity had different dielectric constant values from the crystal asymmetry-dependent reflectivity.~~

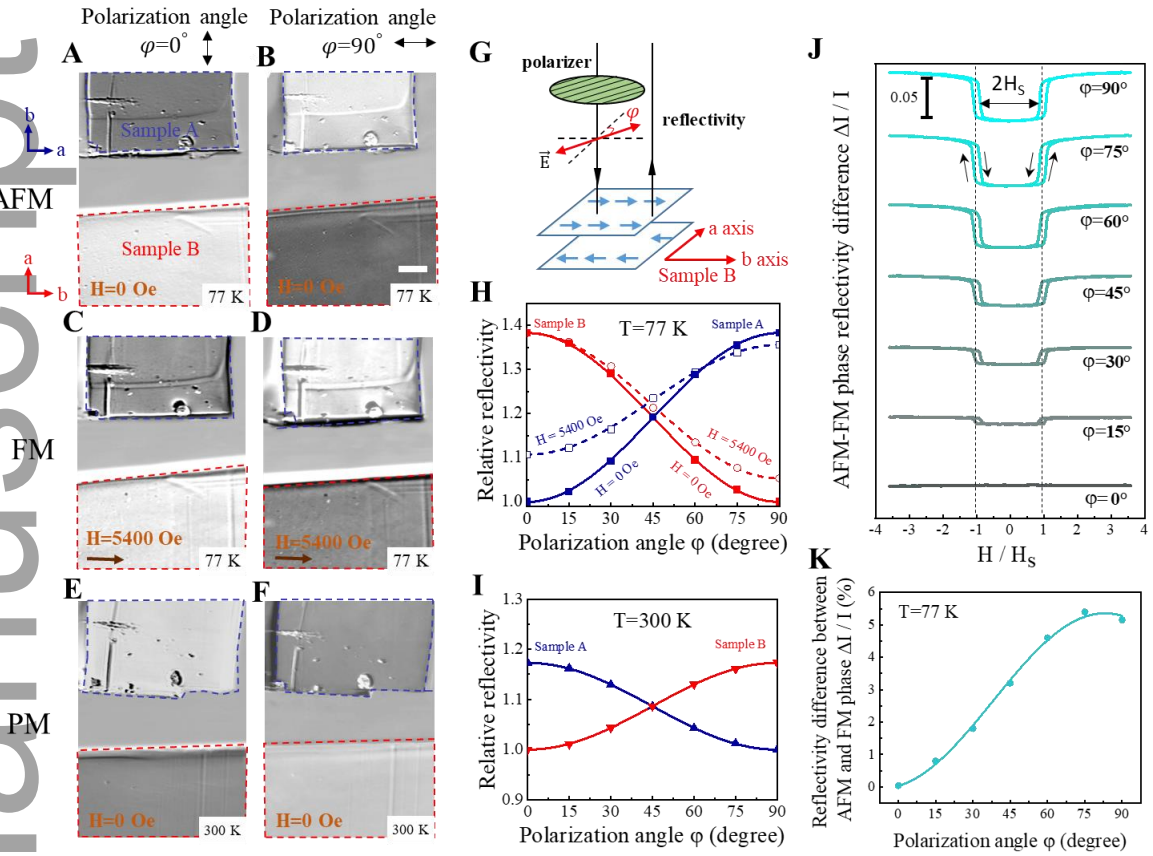

Figure 2. Anisotropic reflectivity of AFM, FM and PM CrSBr. A-F) Magneto-optic image of two samples of CrSBr with the b-axis of sample A (labeled with blue dashed line) aligned vertically and b-axis of sample B (labeled with red dashed line) aligned horizontally, taken with the polarization of normal incident light at (A, C, E) ϕ=0° and (B, D, F) ϕ=90°, respectively. Optical images of CrSBr at (A, B) AFM state (H=0 Oe), (C, D) FM state (H=5400 Oe) at 77K and (E, F) PM state (H=0 Oe) at 300 K were taken. G) Sschematic drawing of measurement geometry with the polarization ϕ defined as the angle between the polarization of incident light and a-axis of sample B. The summarized relative reflectivity as a function of incident light polarization angle ϕ from H) AFM and FM state at 77 K and I) PM state at 300 K from samples A and B, where the relative reflectivity is defined as the ratio of reflected light intensity over that from sample A [AFM state in (H) and PM state in (I)] with polarization of incident light at ϕ=0° (Supplementary Figure S1). J) Ttypical magneto-optic hysteresis loops at various polarization angles, where the jump of reflectivity corresponds to the AFM-FM phase transition. K)

Ssummarized polarization angle dependent reflectivity difference between FM and AFM phase, i.e., ΔI/I from (J). The scale bar indicated in Figure 2B is 40 μm.

Figure 2H and Figure 2I show a quantitative result of the polarization-dependent reflectivity after excluding the background of the polarization-dependent intensity of incident light and slightly adjusting the phase due to sample tilting (Supplementary Figure S1 and Experimental Section). Samples A and B exhibited a clear $\cos^2\phi$ dependence of the polarization angle for all AFM, FM, and PM phases of CrSBr, confirming the uniaxial anisotropic optical properties. Furthermore, the different $\cos^2\phi$ dependences for these three phases indicated that the values of ε_a and ε_b had a strong dependence on the magnetic phases (e.g., AFM, FM, or PM). We noticed that the FM phase has a smaller anisotropy amplitude ($|\varepsilon_a-\varepsilon_b|$) than the AFM phase. To be specific, sample B exhibited identical reflectivities for FM and AFM phases at $\phi=0°$ and a maximum reflectivity difference for FM and AFM phases at $\phi=90°$ (Figure 2H), which is consistent with the theoretical calculation in the next part. To explore the polarization-dependent reflectivity due to the AFM-FM phase transition in CrSBr, the reflected intensity of sample B was measured at different polarization angles as the magnetic field swept along the b-axis (Figure 2J). At $\phi=0°$, the reflectivity had little dependence on the magnetic field. As ϕ increased, the reflectivity exhibited a clear magnetic field dependence which is almost identical to the MOKE loops shown in Figure 1G. The difference in the reflectivity at zero and saturation field (Figure 2K) shows a $\sin^2\phi$ dependence, consistent with the polarization-dependent reflectivity in Fig 2H. Therefore, the hysteresis loops in both Figure 2J and Figure 1G are from the same origin as the reflectivity difference in AFM-FM phase transition. We also noticed that magnetic field of 5400 Oe was not large (almost) enough to align the magnetizations in the field direction along the in-plane hard magnetization axis (a-axis in Figure 2C), leading to a slight difference between the FM phases of sample A and sample B (Figure 2H, Supplementary Figure S1).

To provide a quantitative description of the reflectivity in the AFM and FM phases, we decomposed the polarization of incident light polarization in the ab plane along the a- and b- axes. We define R_φ^F and R_φ^A to be the reflectivity of FM and AFM phases, respectively, at the polarization angle

of ϕ, and n_{aF}, n_{bF}, n_{aA}, and n_{bA} to be the refraction indices for polarization along the a- and b- axes in FM and AFM phase, respectively. Then R_{φ}^{F} and R_{φ}^{A} can be expressed as follows:

$$R_{\varphi}^{F,A} = \left|\frac{1-n_{aF,A}}{1+n_{aF,A}}\right|^2 cos^2\varphi + \left|\frac{1-n_{bF,A}}{1+n_{bF,A}}\right|^2 sin^2\varphi \quad (1)$$

At $\varphi = 0°$, Figure 2H shows $R_{\varphi}^{F} = R_{\varphi}^{A}$ so that $n_{aF} = n_{aA}$. At $\varphi = 90°$, Figure 2H shows $R_{\varphi}^{F} \neq R_{\varphi}^{A}$ so that $n_{bF} \neq n_{bA}$. The polarization angle-dependent reflectivity difference between FM and AFM phase can then be described as $R_{\varphi}^{F} - R_{\varphi}^{A} = [\left|\frac{1-n_{bF}}{1+n_{bF}}\right|^2 - \left|\frac{1-n_{bA}}{1+n_{bA}}\right|^2]sin^2\varphi$, which is consistent with the fitting result shown in Figure 2K.

2.3 Theory revealing of the magneto-optical properties

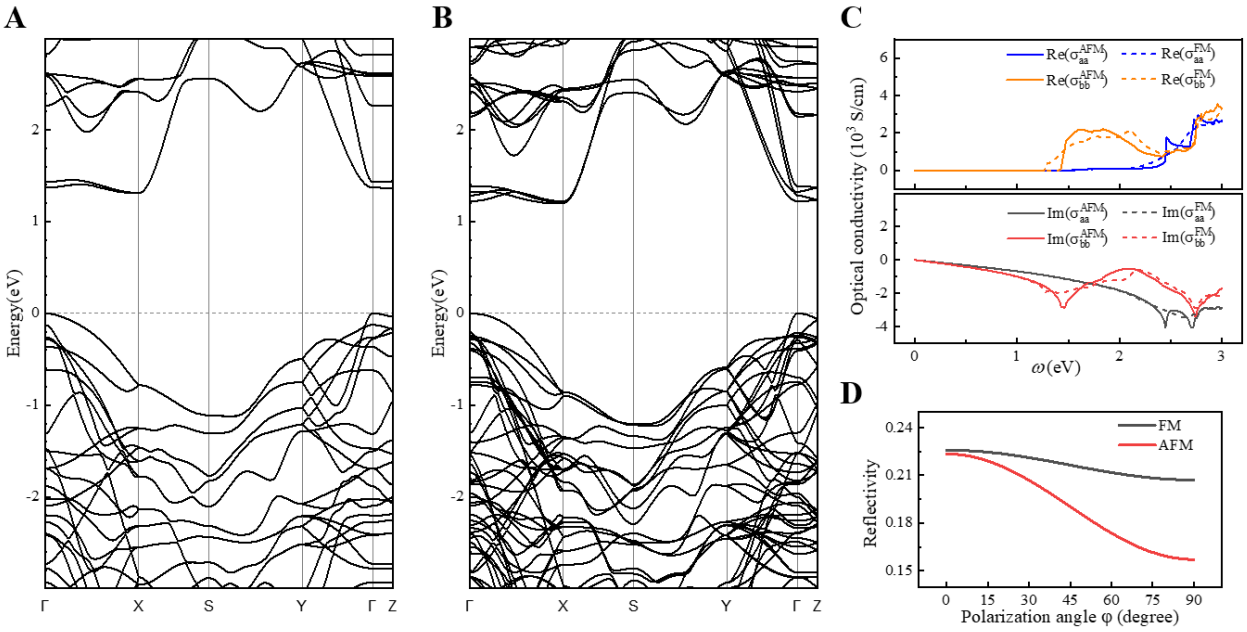

Figure 3. Density functional theory calculations of the optical response of CrSBr. Electronic band structure of CrSBr in A) FM and B) AFM states. C) Ccalculated real part and imaginary part of the optical conductivity as a function of the photon energy. D) Ccalculated reflectivity in CrSBr as a function of polarization angle of incident light with wavelength of 620 nm in FM and AFM states, respectively.

We performed a density functional theory calculation [Experimental Section~~Materials and Methods~~] of the optical conductivity of CrSBr. The band structures in the FM and AFM states are shown in Figure 3A and B, which are consistent with those in previous studies.[23,44] We first numerically confirmed that $\sigma_{ab} = 0$, which is in accordance with the symmetry analysis [Experimental Section~~Materials and Methods~~]. We then calculated the real and imaginary part of σ_{aa} and σ_{bb} as a function of the photon energy in both FM and AFM states, as shown in Figure 3C. By extracting the optical conductivity at 2.0 eV and using Equation (1), we obtained reflectivity at different polarization angles, as shown in Figure 3D. We found the reflectivity in FM state is always larger than that in AFM state. The reflectivity in both FM and AFM states decrease at larger polarization angle of incident light, with a relatively small difference at $\varphi = 0°$ and maximum difference at $\varphi = 90°$, a trend that agrees well with the experimental data shown in Figure 2H.

2.4 Direct imaging of the AFM-FM phase transition in CrSBr

The crystal lattice induced optical anisotropy is related to the angle between light polarization and crystal axis, while the magnetic order induced optical anisotropy is related to the angle between light polarization and spin axis. If we apply a large magnetic field to rotate the spin completely away from b-axis to a-axis, the crystal lattice induced optical anisotropy will remain the same while the magnetic order induced optical anisotropy will be modulated by 90 degrees thus providing a good method to separate the optical anisotropy induced by the lattice from the optical anisotropy induced by the magnetic order at 77 K. Although the equipment does not allow us to apply a magnetic large enough to fully saturate the spin along a-axis, we applied a magnetic field of 5400 Oe (Figs. 2C and 2D) along a-axis and determined the anisotropic reflectivity induced by the crystal lattice, AFM order and FM order combining the results in Figs 2A, 2B and 2H (discussion after Fig. S1 in supplementary file). In Fig. 2C, 2D and 2H, the application of 5400 Oe along a-axis to sample A showed the absence of 90-degree rotation of anisotropic reflectivity, which suggests the contribution of optical anisotropy induced by crystal lattice is larger than that induced by magnetic order at 77 K. We found the crystal lattice induced optical anisotropy changed at different temperatures and showed an opposite sign between 77 K and 300 K (discussion after Fig. S2 in supplementary file), which can be further confirmed

in the temperature-dependent reflectivity in the paramagnetic region of Fig. S2i. Figure 4A shows the spin orientation dependent optical reflectivity ~~in both~~ contributed by the AFM and FM orders ~~phases~~ at 77 K with fixed light polarization along the b-axis ~~after subtracting the background of Figure 2I from Figure 2H~~, demonstrating the realization of optically imaging the AFM Néel vector direction. ~~This process is based on the consideration that the magnetic order-related optical contrast at low temperatures can be obtained after removing the temperature-independent crystal asymmetry part from the overall optical asymmetry. (Supplementary Figure S2), which is similar to the X-ray linear dichroism effect in AFM in that both temperature-dependent AFM order and temperature-independent crystal field contribute to the dichroism.~~[45,46] The reflectivity showed a strong angular dependence on the spin direction ~~relative to the b-axis~~, i.e. both the reflectivity in FM and AFM phases increased as the spin tilts towards a-axis for light with a fixed polarization direction along b-axis. In another word, the deviation of spin orientation away from the light polarization led to larger reflectivity. Moreover, the reflectivity contrast between the FM and AFM phases increases as the spin direction tilts towards the b-axis. This trend fits well with the theoretical prediction of spin ~~angle~~orientation-dependent reflectivity based on symmetry analysis [Experimental Section] ~~[Materials and Methods]~~, which are shown in the solid lines.

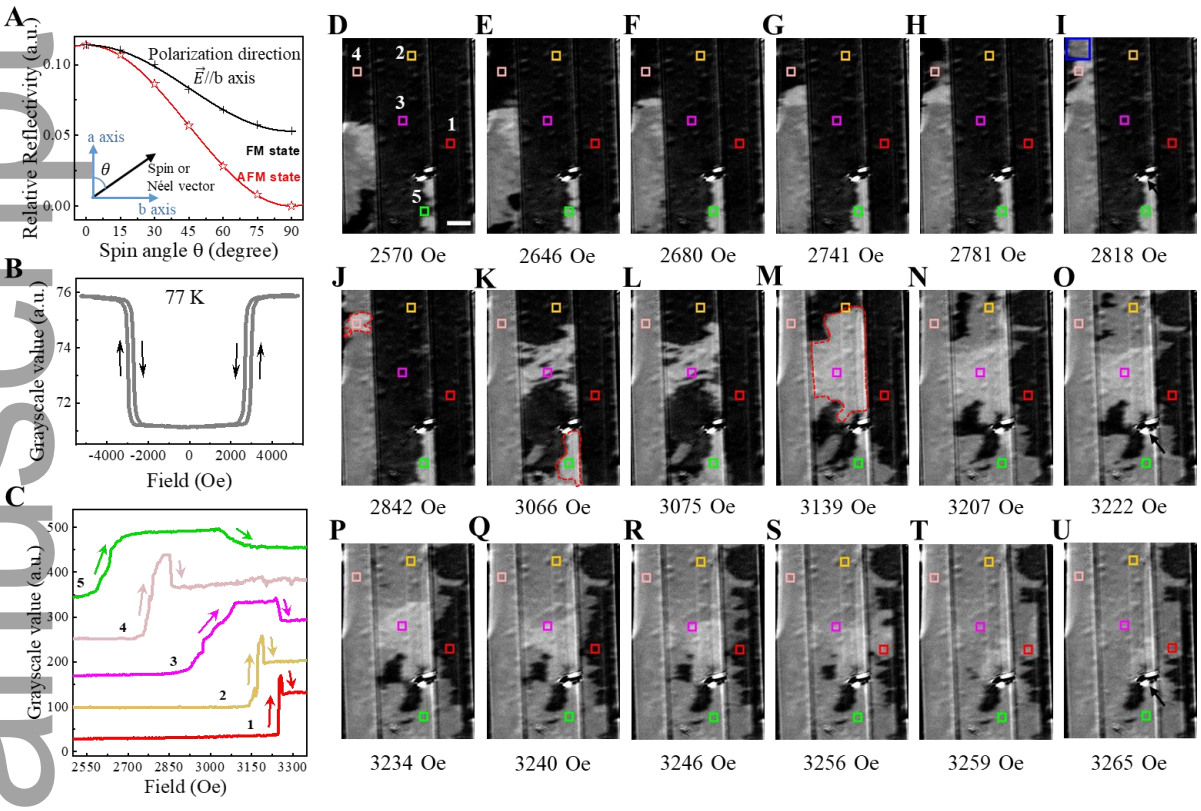

Figure 4. Direct imaging of the domain change during AFM-FM phase transition of CrSBr. A) Reflectivity of CrSBr with fixed polarization direction of incident light along b-axis as a function of spin orientation~~angle~~ in both AFM and FM phases at 77 K. Black cross and red stars are from the experimental result while the solid lines are from theoretical predications based on symmetry analysis. B) H~~h~~ysteresis loop with magnetic field applied along b-axis from the macroscopic averaged signal of CrSBr sample at 77 K. C) F~~f~~ield-dependent grayscale values from selected regions as labeled in (D). Compared with the macroscopic hysteresis loop in (B), the spatially-resolved hysteresis loop in (C) provided more information of the different critical fields and spin configuration changes during the AFM-FM transition from different selected regions. The arrows in (B) and (C) indicate the reflected grayscale change during the field sweeping process. D-U)~~, s~~Selected magnetic domain changes from AFM phase to FM phase for the field increasing from 2570 Oe to 3265 Oe. The red dashed lines in (J, K, M) indicates the additional brighter contrast of white color during the spin-flop transition. The same sample position is indicated as the defects pointed with black arrows in (I, O, U). The scale bar indicated in Figure 4~~3~~D is 30 μm. The grayscale of selected regions changed from dark, to an

intermediate white and finally to gray with increasing magnetic field. For example, the region 3 (labeled as pink square) is dark from 2570 Oe (Figure 4D) to 2991 Oe (Figure 4J), changes to white from 3008 Oe (Figure 4K) to 3132 Oe (Figure 4P), and finally to gray from 3138 Oe (Figure 4Q) to 3150 Oe (Figure 4U).

Based on the unique magneto-optic property, we imaged CrSBr to further reveal the detailed AFM-FM phase transition, where the macroscopic averaged reflectivity showed a sharp transition as the magnetic field swept along the b axis (Figure 4B). Using Kerr microscopy, we captured the domain images throughout the whole process, from the remanent AFM phase to the saturated FM phase, by sweeping the magnetic field at a fine step of 1.5 Oe (Figure 4D-U). We selected 5 different regions to obtain comprehensive information and extracted the grayscale values as a function of the magnetic field. First, we noticed that different regions from different terraces of sample, which has different thicknesses, had different critical fields of the AFM-FM phase transition (Figure 4C). This observation could not be obtained from the macroscopic average measurements. As the magnetic field increased, FM domains (gray color regions in Figure 4) initially nucleated around the sample edges or near defects in the background of AFM domains (dark color regions in Figure 4) and then expanded by domain wall motion to eventually dominate the whole sample region. We speculate the sample edges or the defects can modify the magnetic anisotropy or the interlayer exchange coupling strength, thus lead to variation of spin-flop transition field[30] and cause initial nucleation at these places. We also noticed an interesting phenomenon that the frontside of the domain wall motion always seemed to be accompanied by an additional brighter contrast of color white before the transition of the contrast from a dark color to gray ~~[~~(Supplementary video)~~]~~. In another word, the grayscale of selected regions changed from dark, to an intermediate white and finally to gray with increasing magnetic field. For example, the pink square region (region 3) is dark from 2570 Oe (Figure 4D) to 2991 Oe (Figure 4J), changes to white from 3008 Oe (Figure 4K) to 3132 Oe (Figure 4P), and finally to gray from 3138 Oe (Figure 4Q) to 3150 Oe (Figure 4U). This additional brighter contrast suggests a possible intermediate state of spin-flop transition for CrSBr interlayer AFM spins during the AFM-FM transition process. Spin-flop transition in an AFM means that when a magnetic field is applied along the direction of the spins in a two-sublattice AFM, as the field increases and exceeds a critical value, the spins of both sublattices

suddenly rotate and align almost perpendicular to the field direction in a canted, spin-flop state.[17,18,28,29] During the AFM-FM phase transition of CrSBr, a magnetic field was applied along the b-axis. The spin of CrSBr changed from an AFM phase with spin aligned along b-axis, to a spin-flop state with component of spin orientation along both a- and b-axes, and finally to a FM state with spin aligned along b-axis (Figure 5A). This component of spin orientation along a-axis at spin-flop state should lead to larger reflectivity than the AFM and FM phases with spin along b-axis considering the spin orientation dependence of reflectivity in Figure 4A. Correspondingly, the selected regions should show an enhancement of grayscale values before a sharp decrease, as clearly shown in regions 1 to 5 (Figure 4C). Figure 4J [pink square], K [green square] and M [magenta square] demonstrate the spin-flop transition state [i.e., white color] for regions 4, 5, and 3, respectively. Considering that the spin-flop transition has a sensitive dependence on the magnetic field and only existed in a limited series of frames of images in most cases, the changes in grayscale values of the intermediate spin-flop transition state were only reflected as bumps or spikes in most selected regions. An additional brighter contrast for spin-flop transition state also appeared in the reversed FM-AFM phase transition process with decreasing field strength along the b-axis (Supplementary Figure S3). Besides the thick bulk crystals with the thickness in the order of hundred micrometer, we also observed anisotropic reflectivity associated to different magnetic phases (FM, AFM, or paramagnetic state) and clear spin-flop related domain contrast during an AFM-FM transition on thin flake (Supplementary Figure S5).

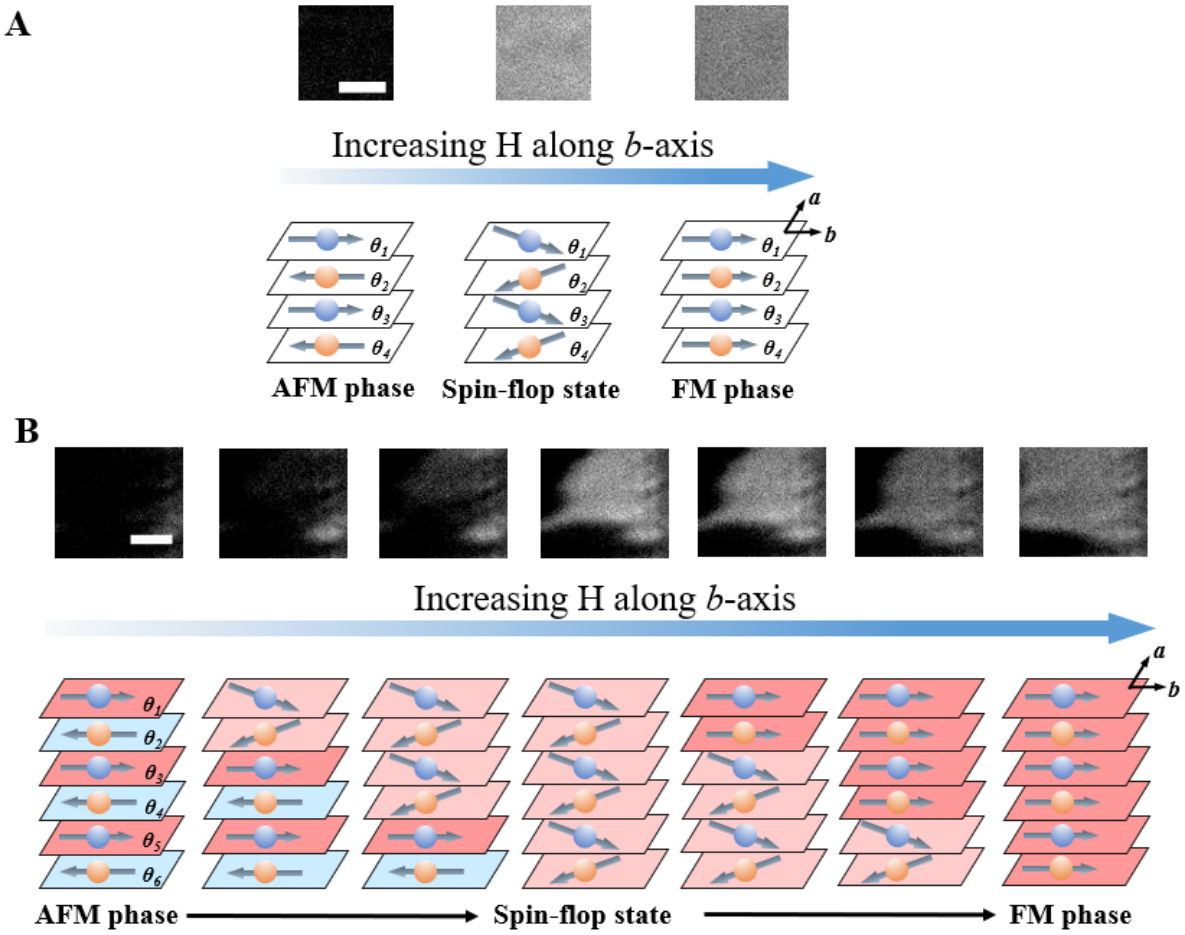

Figure 5. Domain images and corresponding spin configurations during AFM-FM phase transition of CrSBr. A) Sselected domain images from region 3 in Figure 4 and spin configurations for AFM phase, spin-flop state and FM phase. B) Sselected domain images with multiple gray scales from the area labeled with a blue square just above region 4 in Figure 4I, and corresponding spin configurations during the AFM-FM phase transition process. The scale bar is 10 μm.

Based on the spin orientation~~angular~~ dependence of the contrast values in Figure 4A, we were able to determine the spin tilting angle of the spin-flop state in the transition region, which is difficult to obtain in the macroscopic measurement. To capture the important physics without losing generality, as depicted in the schematic drawing (Figure 5A), we made a simple assumption that CrSBr

has uniform (as opposed to a spatial variation of) spin tilting angles relative to the b-axis, which is supported by the numerical calculation (Experimental Section ~~Materials and Methods~~ and Supplementary Figure S4). From the grayscale change in Figure 5A (region 3 of Figure 4c), the spin tilting angle was determined to be ~~24.34°~~20.6° relative to the b-axis for the spin-flop state (discussion after Fig. S3 in supplementary file). We also noticed that multiple domain contrast existed in the AFM-FM phase transition in addition to the white, gray, and dark color domains (e.g., in the area labeled with blue square above region 4). Since the reflectivity measurement probes were quite deep in materials[43] (more than 20 layers of CrSBr), we speculated that this phenomenon might be due to different pinning barriers in different layers, which should yield a layer-dependent critical field for spin flop transition (Figure 5B) and, thus, lead to different grayscales of domain contrast in the field-sweeping process. Depth-dependent switching fields and multistep spin-flop transitions were reported in multilayers[33] and the vdW material $MnBi_2Te_4$,[45~~47~~] respectively. Although we could not pinpoint the particular spin configurations during the AFM-FM phase transition, we also found that multistep spin-flop transitions exist in the in-plane-oriented A-type vdW AFM CrSBr.

3. Conclusion

The experimental and theoretical results presented here revealed a novel magneto-optic effect in vdW CrSBr: different magnetic phases of this material lead to different dielectric anisotropies. Consequently, optical imaging of the anisotropic reflectivity can be used to directly image the AFM spins and the AFM-FM phase transition in CrSBr. This method reveals enormous prospects for the optical imaging of van der Waals antiferromagnets with AFM order-related structural deformation,[46~~48~~] especially for materials with simple in-plane asymmetry, such as uniaxial and four-fold structure. The identification of the spin-flop state and its spin configuration explores the intermediate states of the AFM-FM transition in CrSBr, which enriches our understanding of the AFM-FM phase transition process. The realization of optical determination of the spin orientation and magnetic order in CrSBr establishes this material as a promising candidate for future magnetism control and engineering in 2D AFM spintronics.

4. Experimental Section~~Methods~~

Bulk Crystal Synthesis: A chemical vapor transport method was used to synthesize the high-quality bulk CrSBr single crystals. The stoichiometric mixture of Cr, S, and Br was sealed in a quartz tube under high vacuum. A pre-reaction process was done at 700 °C for 10 hours. Then, a temperature gradient from 850 to 900 °C between the source and growth ends in a two-zone tube furnace was kept for 25 hours. After reversing the temperature gradient and gradually increasing the hot end from 880 to 950 °C, plate- or needle-like CrSBr single crystals can be obtained with lengths up to 2 cm.

VSM measurement: The magnetic properties of CrSBr crystal were measured in a Quantum Design magnetic property measurement system (MPMS3). The mass of CrSBr crystal was calibrated as 0.6 mg. The magnetization of a single crystal of CrSBr was measured as a function of the magnetic field strength with the field applied in a particular orientation with respect to the crystal axes.

Kerr microscopy measurement: We used the commercial Kerr microscopy (Tuotuo Technology) in our measurement. The wavelength of light source is 620 nm and the light was focused down to a 1.2-mm diameter spot on the sample. The low-temperature measurement was performed in a cryostat which was cooled down through the flow of liquid nitrogen. For the hysteresis loops measured with field applied along the in-plane a-axis (Figure 1F) and b-axis (Figure 1G), the measurement geometry is in longitudinal magneto-optical Kerr mode with an oblique p-polarized incident light. For the hysteresis loops measured with field applied along the out-of-plane c-axis (Figure 1H), the measurement geometry is in polar magneto-optical Kerr mode with normal incident p-polarized light. For the measurement of reflectivity in Figure 2 and Figure 4, the polarizer in the path of reflected light was removed as shown in Figure 2G. In the study of magnetic domain imaging of CrSBr, we used a long working distance 20× objective with a 0.42 numerical aperture (NA), i.e. an incident angle of 24.8° relative the normal direction. To remove any influence of topography on the domain imaging, the magnetic domain images in Figure 4 were obtained by subtracting a background image at zero external magnetic field, which is a single domain.

Numerical simulation: The magnetization of each layer is considered as one macrospin following the AFM linear-chain model,[30,45,47,~~4749~~] and spins couple between adjacent layers through interlayer exchange coupling. Considering the exchange coupling energy, magnetic anisotropy energy and Zeeman energy, the total energy can be written as

$$E = \mu_0 M_s[\frac{H_J}{2}\sum_{n=1}^{n=N-1}\cos(\theta_n - \theta_{n+1}) - \frac{H_K}{2}\sum_{n=1}^{n=N-1}(cos\theta_n)^2 - H\sum_{n=1}^{n=N-1}cos\theta_n]$$

where M_s is the saturated magnetization of a single layer and θ_n is the angle of macrospin in the *n*th layer, $H_J = 2J/(\mu_0 M_S)$ and $H_K = K/(\mu_0 M_S)$ are the exchange energy and magnetic anisotropy energy, respectively.

DFT and Wannier calculations: The density functional theory (DFT) calculations were performed using the Quantum Espresso (QE) package.[48~~50~~] Pseudopotentials of all mentioned atoms (Cr, S, and Br) with the generalized gradient approximation (GGA) of Perdew-Burke-Ernzerhof (PBE) functions[49~~51~~] were obtained from the Standard Solid State Pseudopotentials (SSSP) library.[50~~52~~] To add the on-site Coulomb interaction in Cr, the GGA+U method[51~~53~~] was adopted, with U of 4.0 eV and J of 1.0 eV for d orbitals of Cr atom. Long-range van der Waals interactions were captured using DFT-D3 corrections.[52~~54~~] Non-collinear magnetism and spin-orbital effects were also considered. The wave function kinetic energy cutoff and charge density cutoff were set to be 50 Ry and 400 Ry, respectively. A 1×1×2 supercell was constructed to separately describe the FM and AFM structures. The Brillouin zone was sampled by a 17×13×4 Γ-centered Monkhorst-Pack k-point mesh for both self-consistent field (SCF) and non-self-consistent field (NSCF) calculations. The Wannier calculations were performed using the wannier90 code[53~~55~~]. The maximally localized Wannier functions (MLWF) were obtained by projecting the Bloch wave functions from the NSCF calculations using trial orbitals (Cr-d, S-p, and Br-p). The k-point mesh of the Brillouin zone was increased to 170×130×37 through Wannier interpolation, which has been tested and proven to yield converged results. Finally, the optical conductivity mentioned in Figure 3C was obtained using the postw90-berry-kubo module in the wannier90 post-processing program (postw90.x).

Analysis of magnetic space group: Both the MOKE and the optical birefringence are determined by the optical conductivity tensor σ_{ij}. One can divide the optical conductivity into a symmetric and antisymmetric part: $\sigma_{ij} = \sigma_{ij}^{s} + \sigma_{ij}^{as}$. The symmetric part transforms as a rank-two tensor, while the antisymmetric part is equivalent to an axial vector: $\sigma_{ij}^{as} = \epsilon_{ijk} d_k$. To further analyze the form of the optical conductivity, we note that CrSBr has the magnetic space group Pmm'n' and $P_a$nma in its FM and AFM state, respectively. Since both magnetic space groups contain a C_{2b} and M_b symmetry in the corresponding point group, d_z, or in other words, σ_{xy}^{as} is forbidden (the value of σ_{xy}^{as} is zero). This analysis is in good agreement with our experimental result that there is no magnetization-sign dependent MOKE signal. For the symmetric part, the mirror symmetry also forbids σ_{ab}^{s} (the value of σ_{ab}^{s} is zero). As a result, a and b axis are the principal axis, under which σ_{ij}^{s} is diagonal. The birefringence then comes from the anisotropy in the diagonal elements, i.e., $\sigma_{aa} \neq \sigma_{bb}$.

Symmetry analysis of spin orientation~~angle~~-dependent reflectivity: In magnetic materials the order parameter O (FM order or AFM order) can affect the electronic response through the spin-orbit coupling. Therefore, we have $\sigma_{ij}(O) = \sigma_{ij}^{0} + \alpha_{ijk}^{0} O_k + \beta_{ijk\ell} O_k O_\ell + \cdots$,where the coefficients are determined by the crystalline point group. In CrSBr, the mmm crystalline point group requires that $\alpha_{bba}^{0} = \alpha_{bbb}^{0} = 0$ and $\beta_{bbab}^{0} = \beta_{bbba}^{0} = 0$. As the order parameter rotates in the ab plane, we then have $\sigma_{bb} = A\cos^2\theta + B$, with $A = \left(\beta_{bbaa}^{0} - \beta_{bbbb}^{0}\right)O^2, B = \sigma_{bb}^{0} + \beta_{bbbb} O^2$, and θ being the angle between the order parameter and a axis. Since both the refractive index and the reflectivity with the light polarized along the b axis depends on σ_{bb}, we then have $R = R_1\cos^2\theta + R_2$.

Statistical Analysis: In order to study the anisotropic reflectivity of bulk CrSBr in Figure 2, the software of Image J was used to extract the averaged grayscale values of pixels in the selected regions on Sample A and Sample B. We found the grayscale values as a function of the polarization direction of incident light can be well fitted by the formula of $y = a\cos^2(\varphi + b) + c$. The results were analyzed in the following steps. Firstly, since the in-plane crystal axis of the sample is not completely aligned

with the polarization angle of ϕ=0° or ϕ=90°, there is a phase difference which can be corrected by appropriate adjustment of the phase. Secondly, the intensity of incident light changes at different polarization, thus forming a background of the polarization-dependent intensity. We took the average of the grayscale values from sample A and sample B as the background, and subtract the background from the polarization angle-dependent grayscale values. According to that the reflectivity difference between AFM and FM phase was identified to be ~0% and ~5.3% at the polarization angle of 0° and 90°, respectively, the polarization angle-dependent relative reflectivity of Sample A and Sample B was obtained from different magnetic phases (FM, AFM, or paramagnetic state).

Supporting Information

Supporting Information is available from the Wiley Online Library or from the author.

Acknowledgements

The project is primarily supported by National Natural Science Foundation of China (Grants No. 12174364, 12104003, 12241406), the Fundamental Research Funds for the Central Universities (No. wk2310000104), the USTC Research Funds of the Double First-Class Initiative (No. YD2140002004), Users with Excellence Program of Hefei Science Center CAS (No. 2021HSC-UE003), Open Funds of Hefei National Research Center for Physical Sciences at the Microscale (No. KF2021001). Z. Q. Q. acknowledges the support of US Department of Energy, Office of Science, Office of Basic Energy Sciences, Materials Sciences and Engineering Division under Contract No. DE-AC02-05CH11231 (van der Waals heterostructures program, KCWF16), Future Materials Discovery Program through the National Research Foundation of Korea (No. 2015M3D1A1070467), Science Research Center Program through the National Research Foundation of Korea (No. 2015R1A5A1009962), and King Abdullah University of Science and Technology (KAUST) under Award No. ORA-CRG10-2021-4665. Y. G., Z. Y. D. and W. G. Z. are supported by the National Key R&D Program of China (2022YFA1403502, 2019YFA0210004), the Strategic Priority Research Program of Chinese Academy of Sciences (XDB30000000), and Fundamental Research Funds for the Central Universities (Grant Nos.

WK2340000102, WK3510000013). This work was partially carried out at the USTC Center for Micro and Nanoscale Research and Fabrication. This research used resources of Beamlines XMCD-A and XMCD-B (Soochow Beamline for Energy Materials) at NSRL.

J. J. Y., D. X. L. and Z. Y. D. contribute equally to this work. Q. L. and M. Y. designed the experiments, analyzed the data and wrote the paper. J. J. Y. and D. X. L. performed the Kerr microscopy experiments. Y. N. Y. and H. L. P. helped with the Kerr microscopy adjustment. F. F. P., F. J. and L. F. W. helped with the VSM characterization. T. P. M. performed the numerical simulation. Z. Y. D., W. G. Z. and Y. G. performed the DFT calculation. J. Y. Z. and X. L. fabricated the crystals. Z. Q. Q., S. G. W., Y. Z. W. and D. Z. H. contributed to the discussion.

References

[1] C. Gong, L. Li, Z. Li, H. Ji, A. Stern, Y. Xia, T. Cao, W. Bao, C. Wang, Y. Wang, Z. Q. Qiu, R. J. Cava, S. G. Louie, J. Xia, X. Zhang, *Nature* **2017**, 546, 265.

[2] B. Huang, G. Clark, E. Navarro-Moratalla, D. R. Klein, R. Cheng, K. L. Seyler, D. Zhong, E. Schmidgall, M. A. McGuire, D. H. Cobden, W. Yao, D. Xiao, P. Jarillo-Herrero, X. Xu, *Nature* **2017**, 546, 270.

[3] Y. Wang, C. Wang, S. J. Liang, Z. Ma, K. Xu, X. Liu, L. Zhang, A. S. Admasu, S. W. Cheong, L. Wang, M. Chen, Z. Liu, B. Cheng, W. Ji, F. Miao, *Adv. Mater.* **2020**, 32, 2004533.

[4] T. Li, S. Jiang, N. Sivadas, Z. Wang, Y. Xu, D. Weber, J. E. Goldberger, K. Watanabe, T. Taniguchi, C. J. Fennie, K. Fai Mak, J. Shan, *Nat. Mater.* **2019**, 18, 1303.

[5] S. Jiang, L. Li, Z. Wang, K. F. Mak, J. Shan, *Nat. Nanotechnol.* **2018**, 13, 549.

[6] Q. Li, M. Yang, C. Gong, R. V. Chopdekar, A. T. N'Diaye, J. Turner, G. Chen, A. Scholl, P. Shafer, E. Arenholz, A. K. Schmid, S. Wang, K. Liu, N. Gao, A. S. Admasu, S. W. Cheong, C. Hwang, J. Li, F. Wang, X. Zhang, Z. Qiu, *Nano Lett.* **2018**, 18, 5974.

[7] Y. Deng, Y. Yu, Y. Song, J. Zhang, N. Z. Wang, Z. Sun, Y. Yi, Y. Z. Wu, S. Wu, J. Zhu, J. Wang, X. H. Chen, Y. Zhang, *Nature* **2018**, 563, 94.

[8] T. Song, X. Cai, M. W. Tu, X. Zhang, B. Huang, N. P. Wilson, K. L. Seyler, L. Zhu, T. Taniguchi, K. Watanabe, M. A. McGuire, D. H. Cobden, D. Xiao, W. Yao, X. Xu, *Science* **2018**, 360, 1214.

[9] K. Kim, J. Seo, E. Lee, K. T. Ko, B. S. Kim, B. G. Jang, J. M. Ok, J. Lee, Y. J. Jo, W. Kang, J. H. Shim, C. Kim, H. W. Yeom, B. Il Min, B. J. Yang, J. S. Kim, *Nat. Mater.* **2018**, 17, 794.

[10] X. Wang, J. Tang, X. Xia, C. He, J. Zhang, Y. Liu, C. Wan, C. Fang, C. Guo, W. Yang, Y. Guang, X. Zhang, H. Xu, J. Wei, M. Liao, X. Lu, J. Feng, X. Li, Y. Peng, H. Wei, R. Yang, D. Shi, X. Zhang, Z. Han, Z. Zhang, G. Zhang, G. Yu, X. Han, *Sci. Adv.* **2019**, 5, eaaw8904.

[11] Z. Sun, Y. Yi, T. Song, G. Clark, B. Huang, Y. Shan, S. Wu, D. Huang, C. Gao, Z. Chen, M. McGuire, T. Cao, D. Xiao, W. T. Liu, W. Yao, X. Xu, S. Wu, *Nature* **2019**, 572, 497.

[12] T. Yin, K. A. Ulman, S. Liu, A. Granados Del Aguila, Y. Huang, L. Zhang, M. Serra, D. Sedmidubsky, Z. Sofer, S. Y. Quek, Q. Xiong, *Adv. Mater.* **2021**, 33, 2101618.

[13] M. Yang, Q. Li, R. V. Chopdekar, R. Dhall, J. Turner, J. D. Carlstrom, C. Ophus, C. Klewe, P. Shafer, A. T. N'Diaye, J. W. Choi, G. Chen, Y. Z. Wu, C. Hwang, F. Wang, Z. Q. Qiu, *Sci. Adv.* **2020**, 6, eabb5157.

[14] T. Song, Q. C. Sun, E. Anderson, C. Wang, J. Qian, T. Taniguchi, K. Watanabe, M. A. McGuire, R. Stohr, D. Xiao, T. Cao, J. Wrachtrup, X. Xu, *Science* **2021**, 374, 1140.

[15] V. Baltz, A. Manchon, M. Tsoi, T. Moriyama, T. Ono, and Y. Tserkovnyak, *Rev. Mod. Phys.* **2018**, 90, 015005.

[16] T. Jungwirth, X. Marti, P. Wadley, J. Wunderlich, *Nat. Nanotechnol.* **2016**, 11, 231.

[17] S. M. Rezende, A. R. King, R. M. White, and J. P. Timbie, *Phys. Rev. B* **1977**, 16, 1126.

[18] F. L. A. Machado, P. R. T. Ribeiro, J. Holanda, R. L. Rodriguez-Suarez, A. Azevedo, S. M. Rezende, *Phys. Rev. B* **2017**, 95, 104418.

[19] O. Göser, W. Paul, H.G. Kahle, *J. Magn. Magn. Mater.* **1990**, 92, 129.

[20] K. Yang, G. Y. Wang, L. Liu, D. Lu, H. Wu, *Phys. Rev. B* **2021**, 104, 14416.

[21] K. Lee, A. H. Dismukes, E. J. Telford, R. A. Wiscons, J. Wang, X. Xu, C. Nuckolls, C. R. Dean, X. Roy, X. Zhu, *Nano Lett.* **2021**, 21, 3511.

[22] E. J. Telford, A. H. Dismukes, K. Lee, M. Cheng, A. Wieteska, A. K. Bartholomew, Y. S. Chen, X. Xu, A. N. Pasupathy, X. Zhu, C. R. Dean, X. Roy, *Adv. Mater.* **2020**, 32, 2003240.

[23] N. P. Wilson, K. Lee, J. Cenker, K. Xie, A. H. Dismukes, E. J. Telford, J. Fonseca, S. Sivakumar, C. Dean, T. Cao, X. Roy, X. Xu, X. Zhu, *Nat. Mater.* **2021**, 20, 1657.

[24] T. S. Ghiasi, A. A. Kaverzin, A. H. Dismukes, D. K. de Wal, X. Roy, B. J. van Wees, *Nat. Nanotechnol.* **2021**, 16, 788.

[25] F. Wu, I. Gutierrez-Lezama, S. A. Lopez-Paz, M. Gibertini, K. Watanabe, T. Taniguchi, F. O. von Rohr, N. Ubrig, A. F. Morpurgo, *Adv. Mater.* **2022**, 34, 2109759.

[26] J. Cenker, S. Sivakumar, K. Xie, A. Miller, P. Thijssen, Z. Liu, A. Dismukes, J. Fonseca, E. Anderson, X. Zhu, X. Roy, D. Xiao, J. H. Chu, T. Cao, X. Xu, *Nat. Nanotechnol.* **2022**, 17, 256.

[27] W. Liu, X. Guo, J. Schwartz, H. Xie, N. U. Dhale, S. H. Sung, A. L. N. Kondusamy, X. Wang, H. Zhao, D. Berman, R. Hovden, L. Zhao, B. Lv, *ACS Nano.* **2022**, 16, 15917.

[28] A. N. Bogdanov, A. V. Zhuravlev and U. K. Rößler, *Phys Rev B* **2007**, 75, 094425.

[29] B. C. S. Grandi and W. Figueiredo, *Phys. Lett. A* **1989**, 139, 281.

[30] C. Ye, C. Wang, Q. Wu, S. Liu, J. Zhou, G. Wang, A. Soll, Z. Sofer, M. Yue, X. Liu, M. Tian, Q. Xiong, W. Ji, X. R. Wang, *ACS Nano.* **2022**, 16, 11876.

[31] V. Saidl, M. Brajer, L. Horak, H. Reichlova, K. Vyborny, M. Veis, T. Janda, F. Trojanek, M. Marysko, I. Fina, X. Marti, T. Jungwirth, P. Nemec, *New J. Phys.* **2016**, 18, 083017.

[32] T. P. Almeida, D. McGrouther, R. Temple, J. Massey, Y. Li, T. Moore, C. H. Marrows, S. McVitie, *Phys. Rev. Mater.* **2020**, 4,034410.

[33] D. Elefant, R. Schäfer, J. Thomas, H. Vinzelberg, and C. M. Schneider, *Phys. Rev. B* **2008**, 77, 014426.

[34] A. S. J. Stöhr, T. J. Regan, S. Anders, J. Lüning, M. R. Scheinfein, H. A. Padmore, and R. L. White, *Pphys. Rev. Lett.* **1999**, 83, 1862.

[35] F. Nolting, A. Scholl, J. Stohr, J. W. Seo, J. Fompeyrine, H. Siegwart, J. P. Locquet, S. Anders, J. Luning, E. E. Fullerton, M. F. Toney, M. R. Scheinfein, H. A. Padmore, *Nature* **2000**, 405, 767.

[36] W. Chen, Z. Sun, Z. Wang, L. Gu, X. Xu, S. Wu, C. Gao, *Science* **2019**, 366, 983.

[37] J. J. Xian, C. Wang, J. H. Nie, R. Li, M. Han, J. Lin, W. H. Zhang, Z. Y. Liu, Z. M. Zhang, M. P. Miao, Y. Yi, S. Wu, X. Chen, J. Han, Z. Xia, W. Ji, Y. S. Fu, *Nat. Commun.* **2022**, 13, 257.

[38] B. Niu, T. Su, B. A. Francisco, S. Ghosh, F. Kargar, X. Huang, M. Lohmann, J. Li, Y. Xu, T. Taniguchi, K. Watanabe, D. Wu, A. Balandin, J. Shi, Y. T. Cui, *Nano Lett.* **2020**, 20, 553.

[39] D. J. Rizzo, A. S. McLeod, C. Carnahan, E. J. Telford, A. H. Dismukes, R. A. Wiscons, Y. Dong, C. Nuckolls, C. R. Dean, A. N. Pasupathy, X. Roy, D. Xiao, D. N. Basov, *Adv. Mater.* **2022**, 34, 2201000.

[40] V. Saidl, P. Nemec, P. Wadley, V. Hills, R. P. Campion, V. Novak, K. W. Edmonds, F. Maccherozzi, S. S. Dhesi, B. L. Gallagher, F. Trojanek, J. Kunes, J. Zelezny, P. Maly, T. Jungwirth, *Nat. Photon.* **2017**, 11, 91.

[41] J. Xu, C. Zhou, M. W. Jia, D. Shi, C. Q. Liu, H. R. Chen, G. Chen, G. H. Zhang, Y. Liang, J. Q. Li, W. Zhang, Y. Z. Wu, *Phys. Rev. B* **2019**, 100,134413.

[42] J. Xu, H. R. Chen, C. Zhou, D. Shi, G. Chen, Y. Z. Wu, *New J. Phys.* **2020**, 22, 083033.

[43] Z. Q. Q. a. S. D. Bader, *Rev. Sci. Instrum.* **2000**, 71, 1243.

[44] J. Klein, B. Pingault, M. Florian, M. C. Heissenbuttel, A. Steinhoff, Z. Song, K. Torres, F. Dirnberger, J. B. Curtis, M. Weile, A. Penn, T. Deilmann, R. Dana, R. Bushati, J. Quan, J. Luxa, Z. Sofer, A. Alu, V. M. Menon, U. Wurstbauer, M. Rohlfing, P. Narang, M. Loncar, F. M. Ross, *ACS Nano.* **2023**, 17, 5316.

[45] D. Alders, L. H. Tjeng, F. C. Voogt, T. Hibma, G. A. Sawatzky, C. T. Chen, J. Vogel, M. Sacchi, S. Iacobucci, *Phys. Rev. B* **1998**, 57, 11623.

[46] S. Altieri, M. Finazzi, H. H. Hsieh, H. J. Lin, C. T. Chen, T. Hibma, S. Valeri, G. A. Sawatzky, *Phys. Rev. Lett.* **2003**, 91, 137201.

[47] [45] S. Q. Yang, X. L. Xu, Y. Z. Zhu, R. R. Niu, C. Q. Xu, Y. X. Peng, X. Cheng, X. H. Jia, Y. Huang, X. F. Xu, J. M. Lu, Y. Ye, *Phys. Rev. X* **2021**, 11, 011003.

[48] [46] W. L. Roth, *J. Appl. Phys.* **1960**, 31, 2000.

[49] [47] Z. Wang, M. Gibertini, D. Dumcenco, T. Taniguchi, K. Watanabe, E. Giannini, A. F. Morpurgo, *Nat. Nanotechnol.* **2019**, 14, 1116.

[50] [48] P. Giannozzi, O. Baseggio, P. Bonfa, D. Brunato, R. Car, I. Carnimeo, C. Cavazzoni, S. de Gironcoli, P. Delugas, F. Ferrari Ruffino, A. Ferretti, N. Marzari, I. Timrov, A. Urru, S. Baroni, *J. Chem. Phys.* **2020**, 152, 154105.

[51] [49] J. P. Perdew, K. Burke, M. Ernzerhof, *Phys. Rev. Lett.* **1996**, 77, 3865.

[52] [50] G. Prandini, A. Marrazzo, I. E. Castelli, N. Mounet, N. Marzari, *Npj Comput. Mater.* **2018**, 4, 72.

[53] [51] M. Cococcioni, S. D. Gironcoli, *Phys. Rev. B* **2005**, 71, 035105.

[54] [52] S. Grimme, J. Antony, S. Ehrlich, H. Krieg, *J. Chem. Phys.* **2010**, 132, 154104.

[55] [53] G. Pizzi, V. Vitale, R. Arita, S. Blugel, F. Freimuth, G. Geranton, M. Gibertini, D. Gresch, C. Johnson, T. Koretsune, J. Ibanez-Azpiroz, H. Lee, J. M. Lihm, D. Marchand, A. Marrazzo, Y.

Mokrousov, J. I. Mustafa, Y. Nohara, Y. Nomura, L. Paulatto, S. Ponce, T. Ponweiser, J. Qiao, F. Thole, S. S. Tsirkin, M. Wierzbowska, N. Marzari, D. Vanderbilt, I. Souza, A. A. Mostofi, J. R. Yates, *J. Phys. Condens. Matter.* **2020**, 32, 165902.

Table of Contents

Combining magnetic Kerr microscopy and density functional theory calculations, we demonstrate a successful imaging of AFM-FM phase transition in vdW AFM CrSBr based on its unique magneto-optic property. These findings not only offer new insights into the dynamics of AFM-FM phase transition, but also reveal enormous prospects for magnetism imaging and control in 2D spintronics with vdW AFM.

Jingjing Yu, Daxiang Liu, Zhenyu Ding, Yanan Yuan, Jiayuan Zhou, Fangfang Pei, Haolin Pan, Tianping Ma, Feng Jin, Lingfei Wang, Wenguang Zhu, Shouguo Wang, Yizheng Wu, Xue Liu, Dazhi Hou, Yang Gao, Ziqiang Qiu, Mengmeng Yang, and Qian Li

Direct imaging of antiferromagnet-ferromagnet phase transition in van der Waals antiferromagnet CrSBr

ToC figure